The following paper posted here is not the official IEEE published version. The final published version of this paper can be found in the Proceedings of the IEEE Industry Applications Society. Annual Meeting. (41st : 2006 : Tampa, Florida):pp.1941-1948

Copyright © 2006 IEEE.

Personal use of this material is permitted. However, permission to reprint/republish this material for advertising or promotional purposes or for creating new collective works for resale or redistribution to servers or lists, or to reuse any copyrighted component of this work in other works must be obtained from the IEEE.

Design and Experimental Verification of a 50 kW Interior Permanent Magnet Synchronous Machine

Thomas M. Jahns Seok-Hee Han Ayman M. EL-Refaie Jei-Hoon Baek
Department of Electrical and Computer Engineering
University of Wisconsin – Madison
Madison, WI
jahns@engr.wisc.edu seokheehan@wisc.edu elrefaie@research.ge.com jhbaek@wisc.edu

Metin Aydin Mustafa K. Guven
Caterpillar Inc.
Tech Center
Peoria, IL
maydin@ieee.org Guven_Mustafa_K@cat.com

Wen L. Soong
School of Electrical and Electronic Engineering
University of Adelaide
Adelaide, Australia
wlsoong@eleceng.adelaide.edu.au

***Abstract* — This paper presents the design details for an IPM machine designed to deliver 50 kW constant power over a 5:1 speed range extending from 850 rpm to 4250 rpm, with a gradual reduction in the required output power up to 8000 rpm (25 kW). Electromagnetic, thermal, and structural considerations have been included in the design optimization process. The resulting machine is designed with two magnet layers per pole and a distributed stator winding. Special features of the machine include its deep stator slots and four-layer winding, made necessary by the desire to minimize the machine's moment of inertia. Test results available to date demonstrate that the machine is capable of delivering the required output torque and power, and the agreement between the predicted and measured machine parameters is generally quite good. Calculated iron losses for high-speed flux-weakening operation are presented in the final section of the paper, illustrating the challenges associated with minimizing the impact of high-frequency harmonic flux density components.**

Keywords; Interior permanent magnet (IPM) synchronous motor; constant power speed ratio (CPSR); flux weakening; design optimization; cross-saturation; iron losses; prototype machine

I. INTRODUCTION

During recent years, interior permanent magnet (IPM) synchronous machines have emerged from their relative obscurity to become popular choices for high-performance applications such as traction machines used in production hybrid vehicles including the Toyota Prius, Honda Accord, and Ford Escape. This emergence has been driven by a combination of factors including significant reductions in the cost of neodymium-iron-boron (NdFeB) permanent magnets and the attractive performance features of IPM machines that include high power density, high efficiency, and an ability to achieve wide speed ranges of constant-power operation.

The power ratings of IPM machines have been increasing significantly during the past decade from typical values less than 5 kW to power ratings well above 100 kW in order to satisfy the requirements of the desired new applications. Unfortunately, there are very few technical papers that have been presented to date describing the design details associated with these larger IPM machines or their resulting performance characteristics. The small number of papers that have appeared [1,2] provide limited insights into the design features or the measured machine parameters and performance characteristics of these machines.

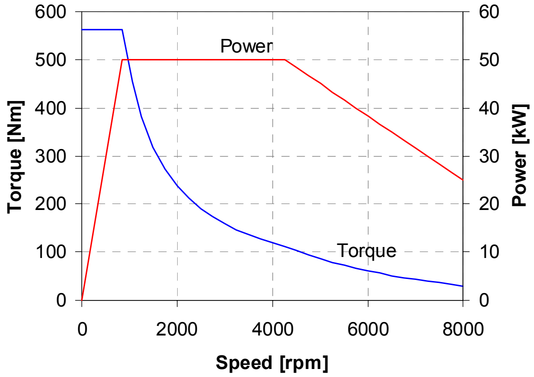

Figure 1. Specified torque-vs-speed and power-vs-speed capability envelopes for the 50 kW IPM machine operating at 150°C.

The purpose of this paper is to present the design details for a 50 kW IPM machine designed to deliver 50 kW constant power over a 5:1 speed range extending from 850 rpm to 4250 rpm, with a gradual reduction in the required output power up to 8000 rpm (25 kW). A plot of the required torque-vs-speed capabilities is presented in Fig. 1 for conditions when the rotor magnet temperature is 150°C.

Discussion is devoted to the interactions between the electromagnetic, thermal, and structural constraints that had to

TABLE I. MINIMUM AND MAXIMUM RANGES OF KEY MACHINE DESIGN PARAMETERS USED IN THE OPTIMIZATION

Parameter	Minimum	Maximum
Magnet remanent flux density B_r [T]	0.725	1.05
Number of pole pairs	3	5
Stator electromagnetic core OD [mm]	220	300
Active stack length [mm]	200	330
Stator yoke back-iron depth [mm]	10	20
Slots/pole/phase	1	3
Short pitching of winding [No. slots]	0	2
Ratio of slot height to width	2	20
Ratio of tooth width to slot pitch	0.3	0.65
Turns per coil divided by number of parallel circuits	2.5	12

be simultaneously satisfied in order to complete the machine design. Fabrication details for the prototype IPM machine are provided, identifying some of the challenges posed by this application. Although testing of this machine has not been completed at the time of this writing, experimental results are presented for characterization of the key IPM machine parameters, including comparisons with predicted values. Experimental verification of the machine's torque production capabilities are presented, concluding with a discussion of iron losses during high-speed flux-weakening operation that will be measured during future tests.

II. IPM MACHINE DESIGN

A. *IPM Machine Design Process*

The electromagnetic design of the 50 kW IPM machine was carried out using a nonlinear lumped-parameter magnetic circuit model of an IPM machine that includes rotor magnetic saturation effects [3]. This model has been embedded in a numerical optimization program that uses differential evolution [4], a relatively new genetic algorithm, to find the best possible machine design to meet the demanding performance requirements. This algorithm was selected because of its attractive convergence and robustness properties for this type of optimization problem [5].

The electromagnetic design optimization entails the variation of 16 different machine parameters within constrained ranges determined by the system requirements. First, candidate electromagnetic designs that meet all of the key performance requirements are identified by the iterative program. Next, an objective function is used to quantitatively rank the machine designs in this eligible subset in order to identify the "best" design. For this application, the scalar objective function consisted of a weighted combination of the stator current for rated torque production, the rotor moment of inertia, and the machine volume.

Table I provides a summary of the ranges over which several of the key machine parameters were allowed to vary during the course of the electromagnetic design optimization. Entries in this table show that the search was limited to conventional distributed stator windings with integral numbers of slots-per-pole-per-phase. The search focused on IPM machines with stack diameter-to-length aspect ratios in a range between approx. 2/3 and 3/2. Sintered high-strength NdFeB magnets were favored by setting the minimum remanent flux density to 0.725 T. Although not included in this table, the search was limited to IPM machines with two magnet layers per pole, a choice that provides a good compromise between electromagnetic design considerations (i.e., magnet vs. reluctance torque) and machine structural/fabrication factors.

A combination of electromagnetic, structural, and thermal finite element analysis (FEA) tools were then used to evaluate and adjust the machine design in order to simultaneously meet the requirements in all three categories. Since the lumped-parameter model (LPM) is not sufficiently accurate to predict the machine's electrical performance by itself, electromagnetic FEA was used in tandem with the numerical optimization to tune key coefficients in the LPM. The iterative process used to accomplish this task is described more thoroughly in a separate paper [7].

Following the completion of the initial round of electromagnetic optimization, the resulting design was subjected to both structural and thermal FEA in order to determine the adequacy of the design to meet requirements in those categories as well. For the structural analysis, it was assumed that the rotor electromagnetic core is mounted on the steel rotor shaft using an interference fit. The resulting manual iterations between the electromagnetic FEA analysis and the structural FEA focused on varying the rotor lamination bridge and center post widths at the ends of the magnet cavities (visible in Fig. 2 below) as well as the interference fit. The challenge in this process is to hold the peak mechanical stresses in the rotor steel laminations within acceptable limits for the material (approx. 350 MPa for M19 steel) at all speeds up to 8000 rpm while minimizing any resulting penalty on the machine's electromagnetic performance.

For the machine's thermal management, it was assumed that lubrication oil at 105°C is the available coolant. As a result of the demanding torque density requirements, the machine has been designed with a stator cooling jacket and a hollow rotor shaft for oil cooling. Sintered NdFeB magnets with favorable high-temperature characteristics were selected in order to achieve the lowest possible machine mass and volume.

The maximum safe operating temperature for the selected magnets is in the vicinity of 175°C to avoid demagnetization, and an effort was made to hold the magnet operating temperature closer to 150°C in order to provide a safety margin. However, this means that the allowable temperature rise of the magnets above the cooling oil temperature is less than 50°C, making the thermal design more challenging.

B. *Resulting IPM Machine Design*

A cross-section of the optimized IPM machine design is provided in Fig. 2, and some of the key machine dimensions are presented in Table II. Design values for several key parameters at 150°C are also included. The optimized machine has 8 poles, with two layers of magnets in each pole.

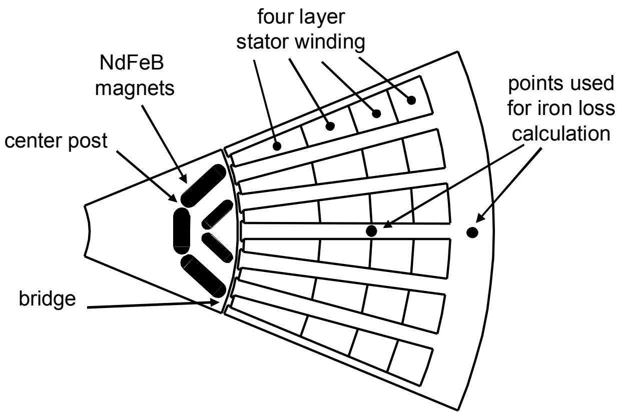

Figure 2. Cross-section of one pole of the 8-pole 50 kW IPM machine

TABLE II. SUMMARY OF KEY DIMENSIONS AND PARAMETERS FOR THE DESIGNED 50 KW PROTOTYPE IPM MACHINE AT 150°C

Rated motoring output power P_R	50 kW
Rated line-to-line phase voltage V_R	480 Vrms
Corner speed ω_R, top speed ω_{Max}	850 rpm, 8000 rpm
Rated torque T_R	562 Nm
Rated phase current I_R	76 Arms
Characteristic current I_{ch}	61 Arms
Shear stress	9.6 psi = 66.2 kPa
Number of poles	8
Stator outer radius	142 mm
Stator inner radius	65.7 mm
Airgap length	0.895 mm
Rotor inner radius	20 mm
Active stack length	322 mm
Magnet remanent flux density B_r	0.994T
Magnet relative recoil permeability	1.045
Stator and rotor lamination material	M19, 29G

Each cavity in the rotor is completely filled with magnets, including the two half-cylinders at each cavity end to help saturate the end bridges and center posts. The cavity ends are smoothly curved in order to minimize the stress concentration associated with angled corners.

The stator slots are quite deep for this design because the objective function placed a high value on minimizing the rotor moment of inertia. The deepness of the slots poses some extra challenges during machine construction, leading to selection of a four-layer stator winding in order to minimize the machine's total active length. Pre-magnetized magnet segments were fabricated in the correct shapes to match the cavity contours.

A view of the fabricated stator and rotor assembly is provided in Fig. 3. Several thermocouples installed in various stator locations are visible. In addition, thermocouples have been installed inside the rotor assembly in contact with the magnets accompanied by instrumentation slip rings that make it possible to monitor the internal rotor temperature during operation. The prototype machine in Fig. 3 is air-cooled. A second prototype machine has been fabricated that includes the previously-noted stator cooling jacket for thermal testing.

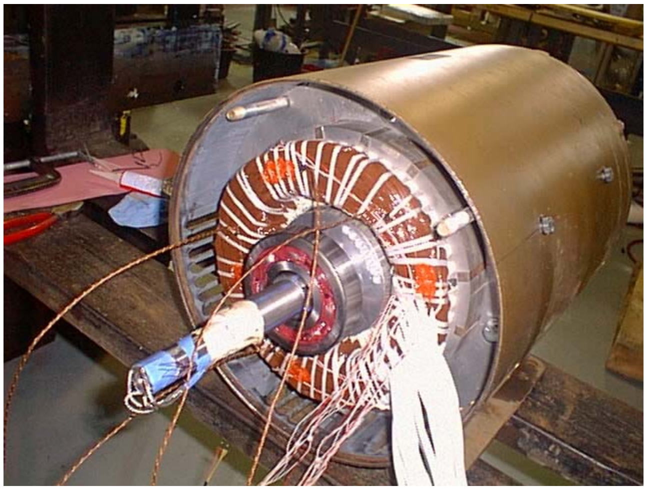

Figure 3. View of completed 50 kW IPM machine stator/rotor assembly

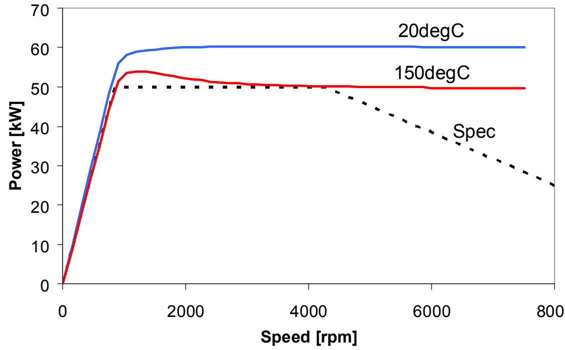

Figure 4. Calculated power vs speed characteristic using the designed value of magnet flux density. (max. allowable phase current of I_R=76 Arms)

Figure 4 shows the calculated power-vs-speed capability envelope for the optimized machine design at 150°C and 20°C, together with the specified envelope. The power-vs-speed curves increase linearly at low speeds below the corner speed and then asymptote to a constant power value at high speed. This high-speed asymptotic power value is proportional to the machine's characteristic current I_{ch} (discussed in more detail below). The overshoot in the calculated power-vs-speed curve that is visible in the 150°C curve near the corner point speed is attributable to the fact that the rated current exceeds the characteristic current [6].

The calculated machine envelopes in Fig. 4 show that high-speed output power is very sensitive to temperature due to the reduction in magnet remanent flux density B_r with temperature. The predicted 17% decrease in magnet flux density associated with the temperature increase from 20°C to 150°C produces a reduction of the high-speed output power by approx. 20%. The output power reduction ratio is greater than the magnet flux density ratio due to the impact of the saturable rotor bridges. More specifically, magnetic saturation of the rotor bridges requires an increasing fraction of the total magnet flux as the value of B_r decreases, causing the bridges to divert a larger percentage of the total magnet flux that otherwise would cross the airgap and couple with the stator windings.

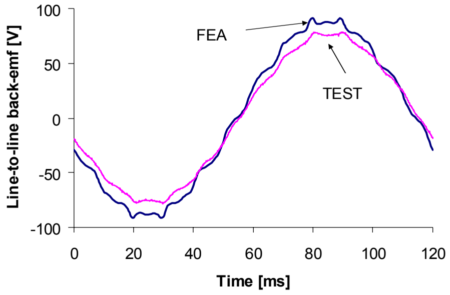

Figure 5. FEA-calculated and measured line-to-line back-emf waveforms for the 50 kW IPM machine at 125 rpm for 20°C operation.

III. IPM MACHINE TEST RESULTS

This section presents the measured electrical parameters and performance characteristics of the prototype machine. Comparisons are provided between these measurements and predictions based on the FEA calculations.

A. Back-EMF Results

Figure 5 presents a measured open-circuit line-to-line back-emf waveform for the prototype 50 kW IPM machine at 20°C together with the FEA-predicted waveform. The calculated THD of the back-emf waveform is 8.3%. The agreement between the waveshapes of the measured and predicted back-emf waveforms is quite good, but there is a significant difference between the amplitudes of these waveforms. More specifically, the FEA-predicted magnet flux linkage λ_{PM} for the machine at 20°C is 13% higher than the measured value (0.694 predicted vs. 0.614 V-s rms).

Tests of some samples of the NdFeB rotor magnets used in the prototype machine indicated that their measured remanent flux density $B_{r(test)}$ is approx. 4.7% lower than their datasheet value $B_{r(design)}$ at 20°C, suggesting that there are additional factors contributing to the shortfall in magnet flux linkage. Other possible reasons for the difference include incorrect rotor lamination bridge/post thicknesses causing greater leakage flux, higher-than-expected saturation flux density B_{sat} values for the lamination iron, or an incorrect airgap length. The last explanation is less likely since the measured q-axis inductance matches the calculated value quite well, as will be shown later in this section.

As a final step, the value of B_r used in the finite-element simulations was manually adjusted to a new lower value $B_{r(adj)}$ to predict nearly the same value of magnet flux linkage as the measured value (see Table III). This represents a 11.9% reduction in B_r compared to the datasheet value at 20°C, and a 7.5% reduction compared to the measured $B_{r(test)}$ values for the tested sample rotor magnets.

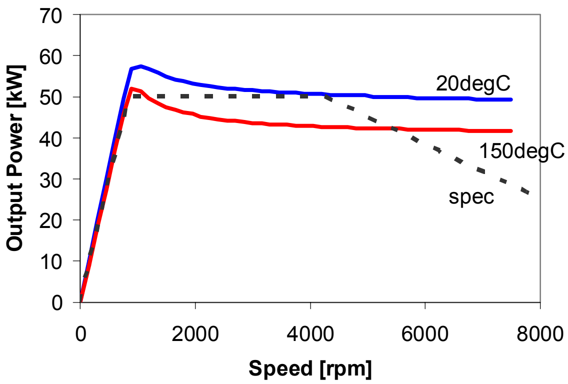

Figure 6. Calculated power-vs-speed capability curve for the 50 kW IPM machine from FE analysis after B_r has been adjusted to $B_{r(adj)}$ to predict the measured magnet flux-linkage. (max. allowable phase current = 84 Arms)

TABLE III. COMPARISON OF PREDICTED AND MEASURED IPM PARAMETERS AT ROOM TEMPERATURE.

Parameter	**L_q Unsat Induct. [mH]**	**L_d Sat'd Induct. [mH]**	**λ_{PM} Flux-Linkage [V-s rms]**	**I_{ch} Char. Current [Arms]**	**I_R Rated Cur. @ 150°C [Arms]**
FEA – $B_{r(design)}$	20.9	9.31	0.694	74.6	76
Measured	23.9	9.75	0.614	63.0	82
FEA – $B_{r(adj)}$	24.1	9.71	0.617	63.6	84

B. Other Machine Parameters

Table III shows a comparison of the measured and predicted machine equivalent circuit parameters for the 50 kW IPM machine at 20°C. The measured machine parameters are shown in the second row. There are significant differences between the predicted and measured inductances and characteristic current when the original design value for the remanent flux density $B_{r(design)}$ is used in the FEA calculations. However, the agreement between the predicted and measured inductances and characteristic current improves considerably when the adjusted value $B_{r(adj)}$ is used in the FEA calculations. This much-improved agreement suggests that the hypothesis of a lower-than-expected effective B_r value in the prototype machine is a very plausible explanation for the differences between the original predicted and measured parameter values when using $B_{r(design)}$.

It can be observed in Table III that changing the value of B_r in the finite element analyses has a significant effect on the unsaturated value of L_q because of magnetic saturation effects. As a result, reducing the magnet remanent flux density to $B_{r(adj)}$ increases the unsaturated q-axis inductance by 10% compared to the original prediction using $B_{r(design)}$. The reduction on B_r also increases the d-axis inductance by 2.5%. In light of this promising agreement, all subsequent finite-element analysis results (e.g. inductance curves, torque, iron loss, etc.) shown in the remaining sections of this paper are based on using the adjusted value of magnet flux density $B_{r(adj)}$.

The lower-than-expected value of magnet flux-linkage increases the rated current I_R required to develop rated torque (562 Nm) at 150°C (see Table III) and reduces the high-speed output power. Figure 6 shows the calculated power vs. speed envelope capability curves based on finite-element analysis

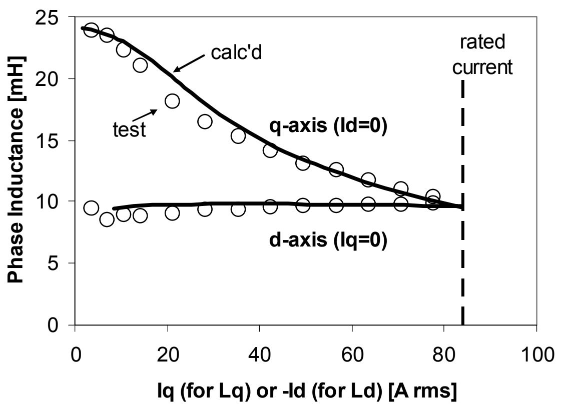

Figure 7. Comparison of measured (circles) and calculated (lines) d- and q-axis inductances without cross-saturation (i.e., $i_q = 0$ for L_d and $i_d = 0$ for L_q).

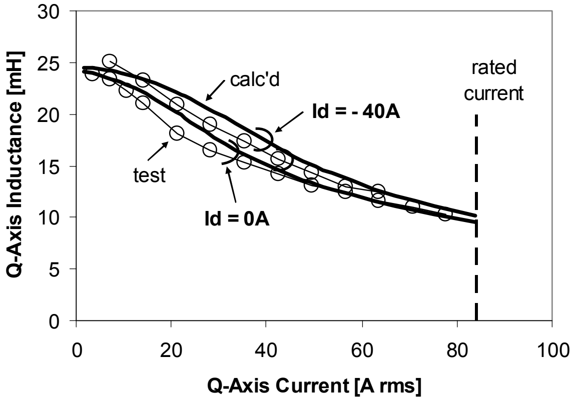

Figure 8. Comparison of measured (circles) and FEA-calculated (bold lines) q-axis inductance L_q illustrating cross-saturation effects for two different values of i_s , 0 and –40 Arms

using $B_{r(adj)}$ and the new higher value of I_R (84 Arms) for the maximum allowable current. These curves show that the prototype machine can still meet the power specifications at 20°C, but will no longer meet the requirements at elevated speeds for 150°C. Increasing the maximum current will not solve this problem since it is caused by insufficient voltage.

C. *Machine Inductances*

Figure 7 shows the measured and calculated variation of the q-axis and d-axis inductances with phase current, excluding the impact of magnetic cross-saturation (i.e., $i_q = 0$ for the L_d curve and $i_d = 0$ for the L_q curve). The measured results show a good correspondence with the FEA-calculated results.

As expected for IPM machines, the q-axis inductance L_q exhibits a significant dependence on i_q because of magnetic saturation. In constrast, the d-axis inductance L_d displays little change with increasing d-axis current. The saliency ratio for this machine is relatively low, having a value of approx. 2.5 under unsaturated conditions ($i_q = 0$), falling to almost unity at high values of q-axis current. This relatively low saliency ratio is attributable, in part, to the unusually deep stator slots and the resulting high leakage inductance caused by the effort to minimize the rotor moment of inertia. The desire to maximize the machine's torque density also has the effect of biasing the IPM machine design in the direction of higher magnet torque and lower reluctance torque (i.e., lower saliency ratio) [7].

Figures 8 and 9 show the impact of cross-saturation on the q-axis and d-axis inductances, respectively. This cross-coupling effect is consistent with the results presented by other authors [8,9]. Figure 8 shows that application of a large negative value of d-axis current (approx. -0.5 pu) causes the q-axis inductance to increase at all values of q-axis current. This is attributable to the fact that the negative d-axis current produces magnetic flux that opposes the flux in the stator teeth contributed by the rotor magnets. This has the effect of lowering the total d-axis flux linkage ($\lambda_{ds} = \lambda_{PM} + L_d\, i_d$) and, hence, increasing the stator iron permeability. The measured results show a good correspondence with the calculated results.

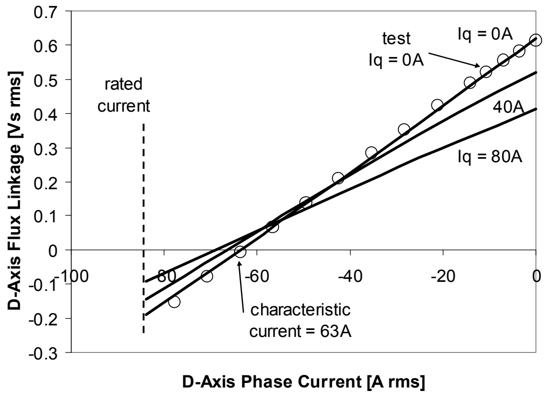

Figure 9. FEA-calculated (bold lines) d-axis magnetic flux linkage λ_{ds} illustrating cross-saturation effects for 3 different values of i_q: 0, 40, and 80 A rms. Test results for zero q-axis current are also shown.

Figure 9 shows the FEA-calculated variation of the d-axis flux linkage λ_{ds} with i_d for q-axis current values of 0, 40, and 80 A rms. Measured test results for the zero q-axis current case show a very good correspondence with the calculated characteristic. The linear variation of λ_{ds} with i_d is consistent with the nearly-constant value of d-axis inductance observed in Fig. 7. The characteristic current I_{ch} corresponds to the value of i_d at which λ_{ds} equals zero, corresponding to a value of approx 63 A rms when the q-axis current is zero.

The results of Fig. 9 show that cross-saturation in the d-axis has the primary impact of reducing the value of L_d (i.e., reducing the slope) as the amplitude of i_q is increased (in either polarity). The value of the magnet flux linkage λ_{PM} (i.e., λ_{ds} @ $i_d = 0$) also exhibits a significant drop due to cross-saturation.

D. *Torque Production*

Since the results in Figs. 8 and 9 show that magnetic cross-saturation has a significant impact on the machine inductances, this effect must be taken into account when calculating the

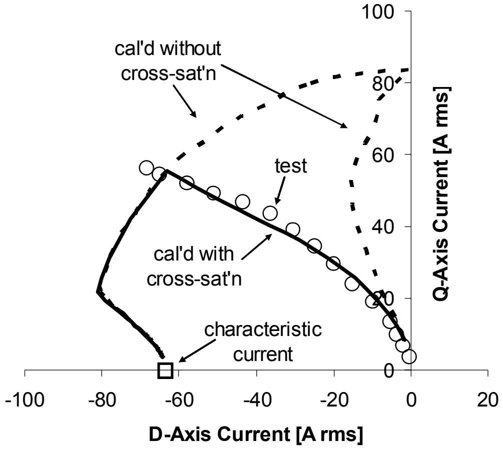

Figure 10. Operating-point trajectory in the i_q-i_d plane showing the calculated result without cross-saturation (dashed line), calculated result with cross-saturation (solid line), and test results below rated speed (circles).

maximum-torque-per-ampere (MTPA) trajectory and output torque. Figure 10 shows the FEA-calculated current operating point trajectory of the machine in the i_q-i_d plane including the effects of cross-saturation during three modes of operation [6]. First, the current increases from zero to rated current (84 Arms) along the MTPA trajectory. Second, the current is maintained at its rated value above rated speed and the current angle is increased to maintain constant voltage (1 pu). Finally, rated current can no longer be maintained at higher speeds, so the operating point moves along the maximum-torque-per-volt (MTPV) trajectory towards the center of the voltage limit ellipse ($i_d = -I_{ch} = -63$ A rms, $i_q = 0$ A).

Figure 10 also plots the calculated operating point trajectory without cross-saturation. For this case, the FEA-calculated inductance curves shown in Fig. 7 are used to obtain the torque for all combinations of i_q and i_d. Those inductance curves show that the machine becomes equivalent to a surface PM machine with an inductance saliency ratio of unity for high values of stator current approaching the rated current value. For surface PM machines, maximum torque-per-ampere is obtained by operating with $i_d = 0$ (i.e., along the i_q-axis). As a result, the trajectory without cross-saturation displays IPM machine behavior when the stator current amplitude is low, but the trajectory veers towards the q-axis when the stator current approaches the rated current value, exhibiting the characteristics of a surface PM machine.

The MTPA trajectory including cross-saturation effects indicates that cross-saturation causes the machine to maintain some value of inductive saliency even at high currents. This occurs because cross-saturation causes L_q to increase (see Fig. 8) and L_d to decrease (see Fig. 9). The measured MTPA trajectory for the prototype IPM machine is also plotted in Fig. 10 and matches this calculated trajectory very well.

Figure 11 provides a comparison of the FEA-calculated and measured torque-vs-current characteristics of the IPM machine along the MTPA trajectory. Rated torque (562 Nm) is developed with a stator current amplitude of approx. 75 Arms @ 20°C. Consistent with the preceding figures, the calculated and measured torque curves demonstrate very good correspondence. The calculated torque-vs-current curve is also plotted for the case ignoring cross-saturation effects. Interestingly, cross-saturation has little net impact on the torque-vs-current curve for this machine because the loss of magnet torque attributable to cross-saturation is offset almost exactly by an increase in the reluctance torque component.

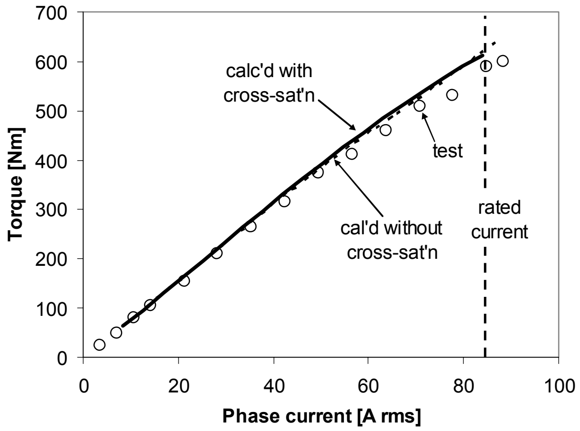

Figure 11. Torque versus phase current for the MTPA trajectory showing calculated results without cross-saturation (dashed line), calculated result with cross-saturation (solid line) and measured test results at 250 rpm (circles).

IV. IRON LOSS ANALYSIS

Stator iron losses can be a significant issue in IPM machines operating over wide constant power speed ranges [10-12]. In particular, the presence of the internal rotor magnet cavities can generate high spatial harmonics in the d-axis armature reaction flux density distribution in the airgap, producing high-amplitude time harmonics in the stator tooth flux density waveforms.

This section describes the use of finite element analysis to calculate the stator tooth and stator yoke flux density waveforms at several operating points along the current trajectory in Fig. 10 (incl. cross-saturation). These correspond to operating along the maximum capability envelope at 750 rpm, 1500 rpm, 4500 rpm and 7500 rpm.

At each operating point, finite element analysis is performed by synchronously stepping the rotor position and the stator current excitation. The stator tooth and yoke positions at which the flux densities are calculated are shown in Fig. 2. The flux density waveforms are then used to calculate the iron loss. The finite element analysis uses the adjusted value of magnet flux density $B_{r(adj)}$ at 20°C for all calculations.

The following iron loss formula for sinusoidal flux density waveforms was obtained by curve fitting the manufacturer's iron loss data at frequencies from 50 Hz to 1 kHz [13]:

$$P = 0.02127 B^{1.641+0.4502B} f + 52.11\times10^{-6} B^2 f^2 \quad \text{[W/kg]} \quad (1)$$

where P is the specific loss in W/kg, B is the peak flux density in Tesla, and f is the frequency in Hz.

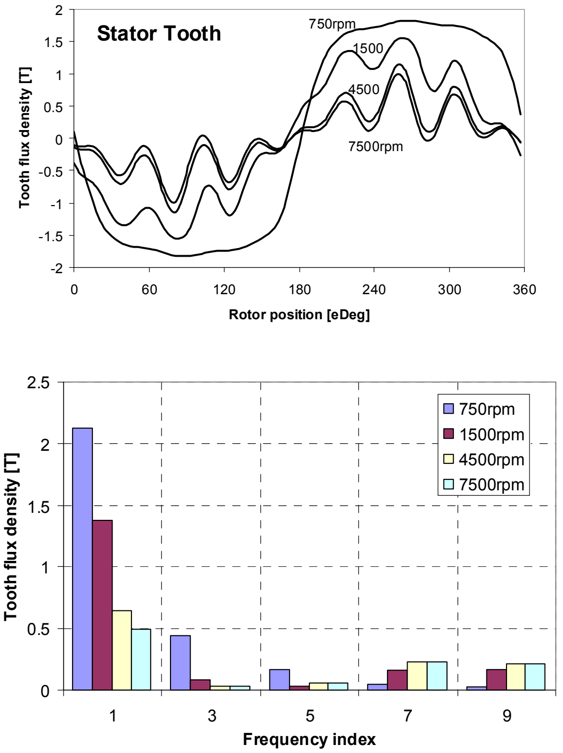

Figure 12. FEA-calculated stator-tooth flux density waveforms (upper) and their frequency spectrum (lower) during operation along the maximum capability envelope at four speeds.

A. *Flux Density Waveform Predictions*

Figure 12 shows the FEA-calculated machine stator-tooth flux density waveforms and their frequency spectra at operating points corresponding to operation along the maximum capability envelope at 750 rpm, 1500 rpm, 4500 rpm, and 7500 rpm. At 750 rpm, the *d*-axis current is nearly equal to the characteristic current, so the stator flux consists largely of the *q*-axis armature reaction flux plus the *d*-axis harmonic components. The harmonic components are not evident in the waveform due to heavy saturation effects.

As the speed is increased, i_d remains relatively constant while i_q falls significantly. This causes the *q*-axis armature reaction flux to fall, reducing the level of magnetic saturation and making the *d*-axis harmonic flux components more evident. It can be seen in the accompanying frequency spectrum that the 7th and 9th harmonic components become significant during flux-weakening operation.

Figure 13 shows the corresponding results for the stator yoke. These waveforms are much more sinusoidal than the stator tooth waveforms even at high speeds. This indicates that the stator tooth losses are likely to dominate the stator yoke losses at high speeds.

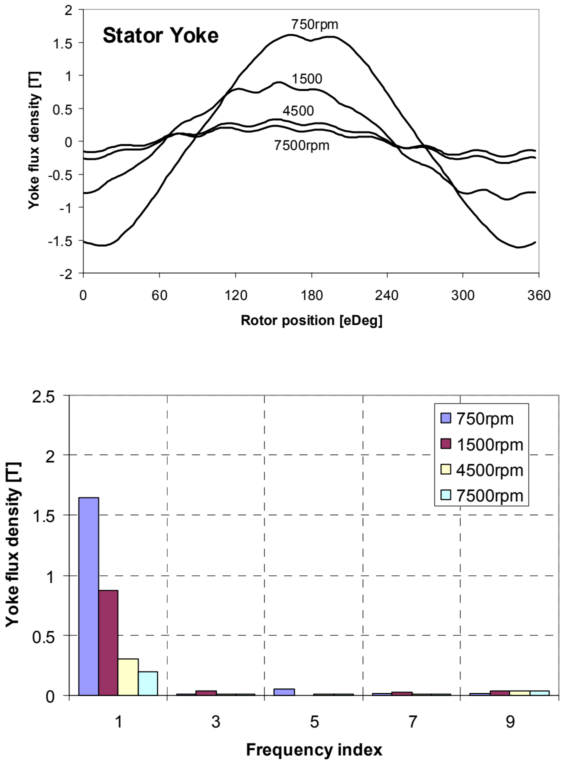

Figure 13. FEA-calculated stator-yoke flux density waveforms (upper) and their frequency spectrum (lower) during operation along the maximum capability envelope at four speeds.

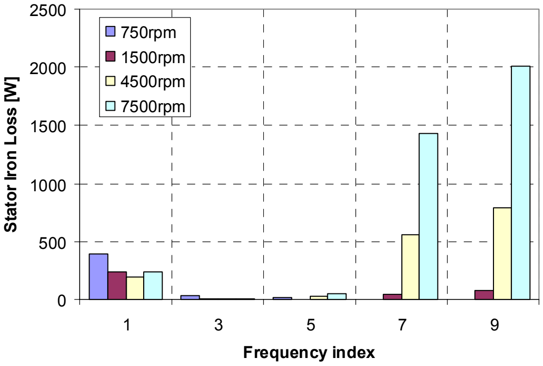

Figure 14. Calculated total stator iron loss harmonic components during operation along the maximum capability envelope at four speeds.

B. *Iron Loss Calculations*

Figure 14 shows the predicted total stator iron losses (sum of tooth and yoke losses) calculated from the frequency spectra shown in Figs. 12 and 13 using the stator tooth and yoke masses and (1). It shows that the fundamental iron loss (frequency index 1) is reduced at high speeds due to flux weakening, but the harmonic iron loss components (particularly the 7th and 9th harmonics) grow quickly and exceed this reduction of the fundamental component.

Figure 15 shows the calculated total losses of the machine at the four test speeds including the breakdown between copper losses and iron losses. It is apparent that stator iron losses dominate the copper losses at high speeds, causing the total losses to increase with rotor speed.

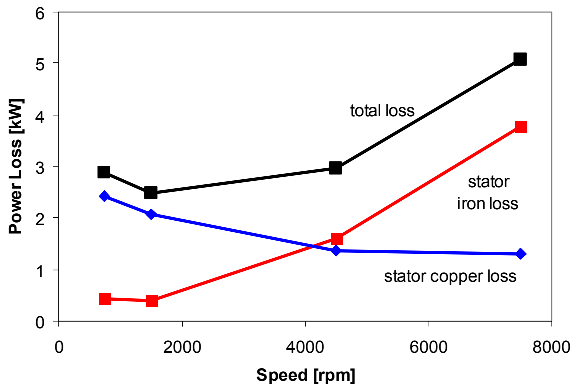

Figure 15. Calculated machine stator copper loss, stator iron loss, and total loss during operation along the maximum capability envelope at four speeds.

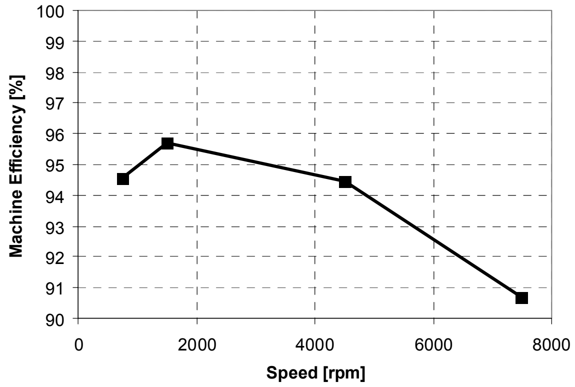

Figure 16. Calculated efficiency of the IPM machine vs speed during operation along the maximum capability envelope.

Figure 16 shows the calculated machine efficiency based on the total losses shown in Fig. 17. Over the constant power speed range (750 rpm to 4000 rpm) the machine maintains a calculated efficiency between 94 to 96% that falls to approx. 90% at maximum speed.

Additional tests are under way to characterize the machine performance at speeds above the corner point, including measurements of the losses and machine efficiency.

V. CONCLUSIONS

This paper has provided insights into the design process and tradeoffs associated with the design of high-performance IPM machines rated to deliver 50 kW output power or higher. Attention is focused on the results of the design optimization exercise for a 50 kW machine designed to achieve a wide speed range of constant-power operation while minimizing the machine's rotor moment of inertia and current rating.

The fabrication and testing of the prototype 50 kW machine and the subsequent comparison between predicted and experimental results provides an appealing opportunity to evaluate both the strengths and limits of current design tools for IPM machines. Key observations include the following:

- The high electric loading and deep stator slots cause heavy stator-tooth saturation, increasing the magnetic cross-saturation effects. Presented results demonstrate the importance of including these cross-saturation effects in determining the max.-torque-per-Amp current trajectory and the resulting machine performance characteristics.
- Calculated results show that iron losses in this machine increase significantly at elevated speeds during flux-weakening operation due to high-frequency stator-tooth harmonics caused by the interaction of the rotor magnet cavities and the stator *d*-axis armature reaction flux.

Additional tests are being carried out to complete the characterization of the prototype machine's performance during operation in the flux-weakening regime beyond the corner point speed. These results will be used to gain further insights into the electromagnetic, structural, and thermal characteristics of this prototype IPM machine that will be helpful in guiding the design of larger (>100 hp) high-performance IPM machines in the future.

REFERENCES

[1] A. Kabasawa, K. Takahashi, "Development of the IMA Motor for the V6 Hybrid Midsize Sedan", SAE Paper 05P-150, 2004.

[2] K. Shingo, K. Kubo, T. Katsu, Y. Hata, "Development of Electric Motors for the Toyota Hybrid Vehicle 'Prius'", in *Proc. of 17th Intl. Electric Vehicle Symposium (EVS-17)*, Montreal, Canada, Oct. 2000.

[3] E.C. Lovelace, T.M. Jahns, J.H. Lang, "A Saturating Lumped-Parameter Model for an Interior PM Synchronous Machine", *IEEE Trans. on Industry Applications*, vol. 38, no 3, May-June 2002, pp. 645-650.

[4] R. Storn and K. Price, "Differential Evolution – A Simple and Efficient Adaptive Scheme for Global Optimization over Continuous Spaces", Tech. Report TR-95-012, Intl. Comp. Sci. Inst., Berkeley, Mar. 1995.

[5] Damir Zarko, "A Systematic Approach to Optimized Design of Permanent Magnet Motors with Reduced Torque Pulsations", PhD Thesis, Dept. of Elec. & Comp. Eng., UW-Madison, 2004.

[6] S. Morimoto, Y. Takeda, T. Hirasa, K. Taniguchi, "Expansion of Operating Limits for Permanent Magnet Motor by Current Vector Control Considering Inverter Capacity," *IEEE Trans. on Ind. Appl.*, vol. 26, Sep/Oct 1990, pp. 866-871.

[7] S. Han, T.M. Jahns, M. Ayden, M. Guven, W.L. Soong, "Impact of Maximum Back-EMF Limits on the Performance Characteristics of Interior Permanent Magnet Synchronous Machines," in *Rec. of IEEE Industry Applications Society Annual Meeting*, Tampa, FL, Oct. 2006.

[8] N. Bianchi and S. Bolognani, "Magnetic Models of Saturated Interior Permanent Magnet Motors Based on Finite Element Analysis," in *Rec. of IEEE Ind. Applications Soc. Annual Meeting*, pp. 27- 34, Oct. 1998.

[9] L. Chedot and G. Friedrich, "A Cross Saturation Model for Interior Permanent Magnet Synchronous Machine. Application to a Starter-Generator," in *Rec. of IEEE-IAS Ann. Meeting*, pp. 64-70, Oct. 2004

[10] V. Zivotic-Kukolj, W.L. Soong, and N. Ertugrul, "Iron Loss Reduction in an Interior PM Automotive Alternator," in *Rec. of IEEE Ind. Appl. Soc. Annual Meeting*, Hong Kong, pp. 1736-1743, Oct. 2005.

[11] F.Magnussen, Y.K. Chin, J.Soulard, A. Broddefalk, S. Eriksson, and C. Sadarangani, "Iron Losses in Salient Permanent Magnet Machines at Field-weakening Operation," in *Rec. of IEEE Ind. Applications Soc. Annual Meeting*, pp. 40-47, Oct. 2004

[12] K. Yamazaki and Y. Seto, "Iron Loss Analysis of Interior Permanent Magnet Synchronous Motors − Variation of Main Loss Factors Due to Driving Condition," in *Proc. IEEE Int. Elec. Mach. & Drives Conf.*, San Antonio, TX, pp. 1633-1638, May 2005.

[13] http://www.cogent-power.com/